Catalysis Science & Technology

PAPER

Study of the local structure and oxidation state of iron in complex oxide catalysts for propylene ammoxidation

Cite this: *Catal. Sci. Technol.*, 2014, 4, 2512

Li-bin Wu,[ab] Liang-hua Wu,[a] Wei-min Yang*[a] and Anatoly I. Frenkel*[b]

Received 14th February 2014,
Accepted 18th March 2014

DOI: 10.1039/c4cy00197d

www.rsc.org/catalysis

Iron molybdate plays a crucial role in the complex oxide catalysts used for selective oxidation and ammoxidation of hydrocarbons but its structural and electronic properties and their changes in the process of the reaction are poorly understood. A combination of Raman, X-ray absorption, and UV-visible spectroscopy was applied to investigate a commercial catalyst as a function of the reaction time. The results show that an iron-containing compound exists predominantly as ferric molybdate in the fresh catalyst, which is reduced progressively in the process of reaction, forming predominantly ferrous molybdate. The irreversible transformation from $Fe_2(MoO_4)_3$ to $FeMoO_4$ was accompanied by formation of a small amount of Fe_2O_3. These two processes observed in our experiment shed light on the deactivation mechanism of this complex catalyst because they have a negative effect on the selectivity and activity. Specifically, they are responsible for the deterioration of the redox couple, blocking the transmission of lattice oxygen, and irreversibly changing the catalyst structure. Based on the results of the combined techniques, a refined procedure has been proposed to develop a more stable and efficient selective oxidation catalyst.

1. Introduction

Selective catalytic oxidation and ammoxidation of hydrocarbons are used in approximately one quarter of the most important industrial chemicals and basic intermediates produced by all catalytic processes worldwide.[1] A molecular-level understanding of catalytic behavior in these processes is important for advancing the general knowledge of catalytic mechanisms and forming a basis for rational design of new catalysts and processes. A major breakthrough in the development of catalysts for oxidation and ammoxidation of olefins was the discovery of the promoting action of iron in the bismuth phosphomolybdate catalyst.[2,3] Although a number of other elements such as Ni, Co, Cr, Mn, and K were later introduced to form the most efficient multicomponent molybdate (MCM) catalyst,[4] iron is still an important promoter in both molybdenum- and antimony-based catalysts.[5] Different chemical forms of iron in molybdate catalysts and its role as a promoter have become subjects of intense research.[6] Early studies by Annenkova *et al.*[7] revealed that $Bi_2(MoO_4)_3$, $Fe_2(MoO_4)_3$, and $Bi_2Fe_4O_9$ are the main components of a Fe–Mo–Bi ternary system. Batist *et al.*[8] reported the formation of $Bi_3FeMo_2O_{12}$ in another Fe–Mo–Bi type system. Wolfs and Matsuura concluded that the maximum activity and selectivity of the $Mg_{11-x}Fe_xMo_{12}BiO_n$ ($0 \le x \le 4$) catalyst is displayed when $x = 2.5$ but did not explain the significance of this optimum iron concentration.[9] Van Oeffelen arrived at the conclusion that the role of iron in the same system is to maintain Bi in the oxidized state by functioning as a redox couple and to maximize activity and selectivity at $x = 2.5$.[10] Consequently, the equation $Bi^{0+} + 3Fe^{3+} \rightarrow Bi^{3+} + 3Fe^{2+}$ was proposed. The role of iron as a Fe^{3+}/Fe^{2+} redox couple was again discussed by Batist.[11] Apart from functioning as a redox couple, iron could also be involved in the formation of other important compounds (as in the case of bismuth molybdate) which can display good activity, selectivity and stability by stabilizing the structure of catalysts.[12]

The time-dependent changes in the catalyst's composition offer a possible explanation for the deterioration of its catalytic activity. Deactivation of the MCM catalyst was attributed to the structural transformation of iron molybdate due to the loss of MoO_3 by volatilization.[13] MoO_3 is mainly formed by reduction of $Fe_2(MoO_4)_3$ in the redox catalytic process according to the equation: $Fe_2(MoO_4)_3 \rightarrow 2FeMoO_4 + MoO_3 + [O]_{lattice}$, evidenced by the presence of a mixture of $Fe_2(MoO_4)_3$ and Fe_2O_3 in similar catalysts.[14] The iron oxide formed by oxidation of ferrous molybdate promotes propylene deep oxidation, deterioration of catalyst activity, target product degradation and is responsible for the reddish-brown

[a] *Shanghai Research Institute of Petrochemical Technology, 1658 Pudong Beilu, Shanghai 201208, China. E-mail: yangwm.sshy@sinopec.com*
[b] *Physics Department, Yeshiva University, New York, NY 10016, USA. E-mail: anatoly.frenkel@yu.edu*

color of the spent MCM catalysts. Additionally, the increasing loss of the reversible Fe^{3+}/Fe^{2+} redox couple or $Fe_2(MoO_4)_3$ structure collapse can also lead to other adverse consequences, such as the increasing pressure drop in the catalytic bed, degradation of the catalyst mechanical resistance, and the decreasing residual activity of MCM.[15]

It is evident from the prior results that the main challenges to a better understanding of the role of iron in this important class of catalysts are the heterogeneity of the chemical states of iron, the coordination environments around iron atoms and their changes during the reaction. This complexity presents significant challenges for their structural and chemical analyses due to the ensemble-average nature of most characterization techniques. In this work, we report a combined use of X-ray absorption fine structure (XAFS) spectroscopy, Raman spectroscopy and diffuse reflectance UV-visible light (DR-UV-vis) spectroscopy for determining the dominant chemical states and functional forms of Fe and their changes during the reaction process in a representative commercial catalyst. The methods used in our work were found to be useful for multi-technique studies of complex catalysts.[16,17] XAFS is known for its excellent sensitivity to chemical and coordination environments of iron complexes,[18] and it is used extensively for analysis of the degradation of MCM catalysts. Similar to other ensemble-average techniques such as XRD, XAFS is not sensitive to minority species because it is a volume-average method. Raman spectroscopy, on the other hand, is capable of detecting such species due to various selection rules.[19] For example, small amounts of MoO_3 mixed into a ferric molybdate-rich phase may not be detectable by XAFS or XRD, but would be detectable by Raman spectroscopy which is used extensively for studying the structure of molybdates.[20] In addition, the fact that the reduced form of iron molybdate, iron oxide, has no significant contribution to the Raman spectrum due to its weak Raman scattering and is sensitive to DR-UV-vis spectroscopy should also be taken into consideration.

Another important aspect of catalysis investigations that this work helps to resolve is the issue of heterogeneity of different chemical forms of the same element in the sample. Ensemble average techniques such as XAFS, when used alone, cannot discriminate between the different models: 1) changes in the chemical states of Fe occur uniformly throughout the entire sample or 2) the sample has a mixture of the same two or more states of Fe at all times, and the volume fraction of each state changes with time.

Our work shows that correlating the results of these techniques is required in order to resolve this challenge, and we propose a specific model of chemical and structural transformation in iron species and shed light on the mechanism of the catalyst deactivation.

2. Experimental

2.1 Catalyst preparation and catalytic tests

The catalyst in this study is a member of the family $Bi_{0.5-1}Fe_{2-3}Mo_{12-14}X_mO_{40-50}$ (ref. 21 and 22) (denoted hereafter as Fe–Mo–Bi) from the Shanghai Research Institute of Petrochemical Technology (SRIPT) which shows high activity and acrylonitrile selectivity at 380–450 °C. X_m stands for other elements such as Cr, Co, Ni, Mg, Mn and K. The catalyst was synthesized using a co-precipitation method; it was then spray dried and calcined in a rotating furnace at a temperature of ~600 °C. Catalytic ammoxidation processes were studied in a Commercial Fluidized Bed Reactor (CFBR) at the SRIPT. After 5 to 10 days of use for the ammoxidation reaction in the CFBR, the catalytic activity reached a stable state. Then the catalyst was studied at the accelerating activity test facilities that employ a Laboratory-scale Fluidized Bed Reactor (LFBR). Using the LFBR, the samples were studied at different times of reaction: fresh (unused), 5 days, 8 days, 11 days, 16 days and 48 days from the beginning of the reaction. The corresponding samples were denoted as S0, S5, S8, S11, S16 and S48, respectively.

2.2 Raman spectroscopy

The metal oxide phase present in the MCM catalyst samples was examined using a Jobin-Yvon LabRam 1B Raman spectrometer. Before measurement the spectrometer was calibrated using a silicon wafer to a wavelength accuracy of ±1 cm^{-1}. The Raman spectra of the fresh and spent catalysts at different reaction times were then collected under ambient conditions using a 632.8 nm excitation line of an He–Ne laser source, equipped with a confocal Olympus microscope (BX-30). The laser power was kept below 0.5 mW so as to minimize any laser-induced alterations of the sample.

2.3 Diffuse reflectance UV-vis spectroscopy

Diffuse reflectance UV-visible spectra of selected samples were obtained (from 12 500 to 50 000 cm^{-1}) using a Perkin Elmer 555 double beam spectrophotometer at the SRIPT. $BaSO_4$ was used as the reference and the slit width was set to 2.0 nm.

2.4 X-ray absorption spectroscopy

Fe K-edge X-ray absorption spectroscopy (XAS) data were collected in transmission mode at the beamline X-19A of the National Synchrotron Light Source in Brookhaven National Laboratory in New York, USA. A double crystal Si (111) monochromator was detuned by 30% to minimize the effect of harmonics. Gas-filled ionization chamber detectors were used for measuring incident and transmitted beam intensities. In addition, a third ionization chamber was used to detect the beam through a reference Fe foil for energy calibration and data alignment purposes. The XAS specimens were made by depositing the catalyst powders onto adhesive tapes and folding the tape several times for homogeneity. The edge steps of the X-ray absorption coefficient at the Fe K-edge energy varied between 0.3 and 0.4 for all samples.

Initial data processing was performed by the Athena[23] software from the IFEFFIT data analysis package. Several consecutive measurements of the same sample were aligned and

averaged to minimize statistical noise in the data. To directly compare X-ray Absorption Near Edge Structure (XANES) data of different samples, the same procedure of pre-edge line fitting, post-edge curve fitting, and edge-step normalization was applied to all samples. Quantitative data analysis was done using the PCA software.[24,25]

3. Results

3.1. Raman spectroscopy

The spectra corresponding to different reaction times are shown in Fig. 1. The spectra feature a symmetric stretching mode, ν_1, of the MoO_4 tetrahedron at 955 cm^{-1}, an asymmetric stretching mode at 890 cm^{-1} and/or 835 cm^{-1}, bending modes in-plane and out-of-plane at 430 and 360 cm^{-1}, and rotation of the entire tetrahedron at 240 cm^{-1}. These observations are in good agreement with the literature.[26–29] Similar spectra have been obtained for β-$CoMoO_4$ where ν_1 = 945 cm^{-1}, Ni/Mo alloys (ν_1 = 940 cm^{-1}),[26] β-$HgMoO_4$ (ν_1 = 970 cm^{-1}), α-$MnMoO_4$ (ν_1 = 940 cm^{-1}), and $NiMoO_4$ (ν_1 = 960 cm^{-1}).[27] Vibrational modes of MoO_4 have been reported at 700–900 cm^{-1} and its bending modes at 300–400 cm^{-1}.[28] The spectra shown in Fig. 1 also reveal the presence of $Fe_2(MoO_4)_3$ in our catalyst, which has a characteristic high intensity and well isolated band at 783 cm^{-1}. This is in good agreement with the reported data for $Fe_2(MoO_4)_3$ that feature major bands at 960, 780, and 350 cm^{-1}.[20,29] Quantitatively, the 783 cm^{-1} peak intensity can thus be used for estimating the amount of $Fe_2(MoO_4)_3$ in our catalysts. Fig. 1 demonstrates that this compound exhibits a gradual decrease in its quantity with reaction time. Therefore, our Raman measurements, in agreement with previous reports,[30] indicate that the majority of iron exists in the form of $Fe_2(MoO_4)_3$ in fresh catalysts (as well as in short service time catalysts) and its reduction to $FeMoO_4$ after long-time use. This result is only a partial picture of the composition and structure of the Fe–Mo phase in the catalyst because other Fe phases that are not Raman-active may also be present.

As demonstrated in Fig. 1, $Fe_2(MoO_4)_3$ shows abundant load in S0, then its amount decreases monotonically in S5 through S48. For semi-quantitative purposes, the intensity ratio was calculated between the strongest bands, from $MMoO_4$ (M = Co, Ni, Mn) and $Fe_2(MoO_4)_3$ appearing at ~950 cm^{-1} and 783 cm^{-1}, respectively, assuming that the majority of $MMoO_4$ phases don't change significantly. The values of 0.56, 0.39, 0.35, 0.28, 0.20 and 0.20 for S0, S5, S8, S11, S16 and S48, respectively, demonstrate that the $Fe_2(MoO_4)_3$ phase has been decomposing during the reaction process, from the sample with the highest catalytic activity (S0) in the very beginning to the most deactivated sample (S48) with the longest service time. We will discuss the reason for this decomposition in greater detail below.

As for MoO_3 discussed above, it has its characteristic band at 817 cm^{-1} which is clearly missing from the data in Fig. 1.[31] The absence of the MoO_3 phase from all samples (S0 through S48) is quite reasonable due to their prolonged (5 to 10 days) treatment in the CFBR and high volatility of MoO_3 during the reaction process.[13] As discussed in the Raman spectroscopy section, the amount of $Fe_2(MoO_4)_3$ gradually decreased with reaction time, but what exactly happened to $Fe_2(MoO_4)_3$ remains unclear. The next section will address this question.

3.2. X-ray absorption near edge structure

Fig. 2 shows Fe K-edge XANES spectra collected from the Fe–Mo–Bi catalysts. The spectra of all samples, from S0 to S48, exhibit a gradual shift towards lower energy with the increase of the reaction time. By comparing our data with those previously reported,[32,33] we firmly believe that this trend is consistent with the change in the average oxidation state of Fe from +3 to +2.

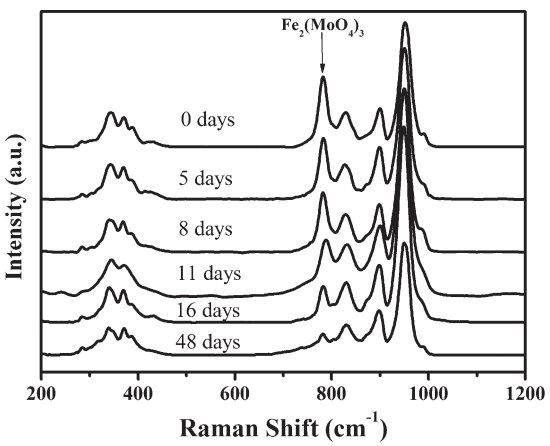

Fig. 1 Raman spectra of Fe–Mo–Bi catalysts corresponding to different times after the beginning of the reaction (0, 5, 8, 11, 16, 48 days). The arrow indicates a peak corresponding to the $Fe_2(MoO_4)_3$ complex.

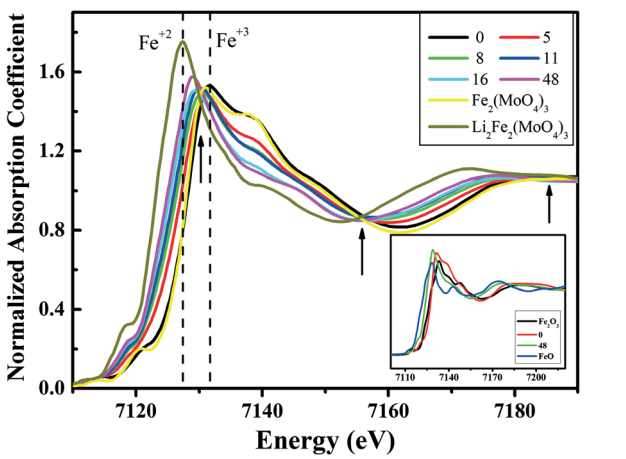

Fig. 2 Fe K-edge XANES of Fe–Mo–Bi catalysts at different reaction times and reference compounds $Fe_2(MoO_4)_3$, $Li_2Fe_2(MoO_4)_3$, Fe_2O_3 and FeO. Arrows show the presence of quasi-isosbestic points indicating both the one-step transformation within the catalysts from S0 towards S48 and their agreement with the two standards, ($Fe_2(MoO_4)_3$, and $Li_2Fe_2(MoO_4)_3$).

Fig. 2 and its inset show dramatic changes in the Fe K-edge XAS data for the different stage catalysts and reference compounds, $Fe_2(MoO_4)_3$, $Li_2Fe_2(MoO_4)_3$, Fe_2O_3 and FeO. The catalyst data and the $Fe_2(MoO_4)_3$, $Li_2Fe_2(MoO_4)_3$, and Fe_2O_3 references were obtained in two different experiments (the reference compounds were measured by Shirakawa *et al.*[32]). In order to directly compare them, all data were first aligned in absolute energy using the reference data of a Fe foil (in the case of the catalyst samples) and Fe_2O_3 (in the case of $Fe_2(MoO_4)_3$ and $Li_2Fe_2(MoO_4)_3$) measured simultaneously with all of the samples. By measuring the XAFS data for the Fe foil and Fe_2O_3 in the same transmission experiment we obtained the relative shifts needed for all data sets to share the same X-ray energy origin.

A nearly perfect agreement between the starting sample, S0, and $Fe_2(MoO_4)_3$ demonstrates that: 1) the charge state of Fe ions was +3 in the fresh catalyst and 2) its Fe phase was predominantly $Fe_2(MoO_4)_3$. The absorption edge positions are defined as the main absorption peak maxima throughout this article. For the $Fe_2(MoO_4)_3$ and S0 data, the Fe K-edge positions are at 7131.8 eV and 7131.5 eV, respectively. Upon catalytic reaction for some period of time, the spectra shifted to lower energies towards the reduced form of iron molybdate, $FeMoO_4$, with the charge state of Fe equal to +2. Instead of measuring $FeMoO_4$, we compared our data with another Fe^{+2} compound of $Li_2Fe_2(MoO_4)_3$ (ref. 34) which has the same local structure around Fe as in $FeMoO_4$.[35] As shown in Table 1, the distributions of the first shell Fe–O distances and the second shell Fe–Mo distances around Fe as well as the coordination environment in these two compounds are very similar. Hence, the use of $Li_2Fe_2(MoO_4)_3$ for comparing with the experimental data for the Fe–Mo–Bi catalysts is justified.

In the spectra of the last sample, S48, its Fe K-edge energy (7129 eV) is higher than that of $Li_2Fe_2(MoO_4)_3$ (7127 eV), as shown in Fig. 2. Hence, the average charge state of Fe in the last sample is not equal to but approaching the value of +2. As evidenced by the presence of quasi-isosbestic points in Fig. 2, Fe ions in all samples undergo transformation from ferric molybdate to ferrous molybdate other than iron oxide, FeO, since its spectroscopic features are different from both S0 and S48.

One possible method of quantitative analysis of these XANES spectra is by linear combination analysis. In this method, data are represented as a linear combination of two or more standard compounds and their mixing fractions correspond to the volume fractions of the corresponding iron species in the sample. The problem with this method is that it does not offer a model-independent determination of the number of independent species. Principal Component Analysis (PCA) is a superior method for that purpose because it allows to 1) find the number of independent species mixed together in the sample at all reaction times and 2) obtain their unique identities.[25,36]

Fig. 3(a) shows the "scree test", demonstrating that the number of principal components required to reproduce all 6 experimental spectra is equal to 2, as evidenced by the negligible eigenvalue (0.005) there. The standard compounds of $Fe_2(MoO_4)_3$ and $Li_2Fe_2(MoO_4)_3$ were well reproduced by the combination of the two principal components and the target transform was performed from the basis of the abstract components to the basis corresponding to the two standards. The mixing fraction of the Fe^{+3} and Fe^{+2} states was obtained using a linear combination fit using the PCA software package.[37] Data reproduction of the experimental spectra and the two standards is shown in Fig. 3(b) as an example.

We have also tested a three-species model against our experimental data, using Fe_2O_3 as a possible standard, in

Table 1 Relevant structure parameters of $FeMoO_4$ (ref. 35) and $Li_2Fe_2(MoO_4)_3$ (ref. 34)

Fe environment	$FeMoO_4$	$Li_2Fe_2(MoO_4)_3$	Difference
Charge valence	+2	+2	0
Fe–O coordination number	6	6	0
Fe–Mo coordination number	6	6	0
Average Fe–O distance (Å)	2.14	2.12	<1%
Average Fe–Mo distance (Å)	3.61	3.67	<2%

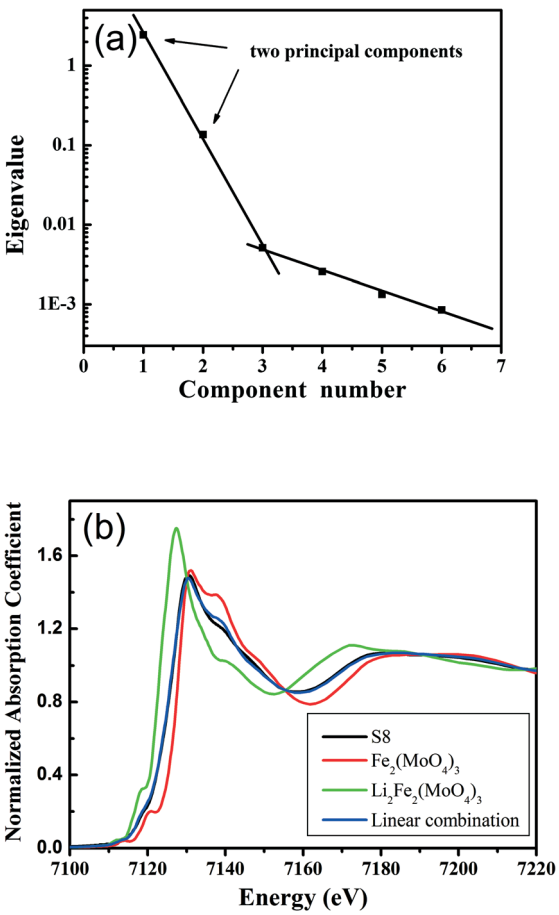

Fig. 3 (a) The "scree test" shows the change trend of the eigenvalues obtained by principal component analysis. The change in slope after the two leading eigenvalues indicates that the number of independent species in the sample is equal to 2. (b) The representative linear combination fit of sample S8 using the standard trends of $Fe_2(MoO_4)_3$ and $Li_2Fe_2(MoO_4)_3$. Their mixing fraction was the only fitting variable.

addition to the previous two-species standards as described above. The best fit values of the mixing fractions, corresponding to species after the target transform procedure, had large negative values, which is non-physical. Hence, our XANES data gave no evidence for the formation of Fe_2O_3 within the accuracy of the PCA method used.

Guided by the PCA results, we treated the changes of the Fe oxidation state in the catalyst during the reaction as a one-step transformation from Fe^{+3} to Fe^{+2} and summarized the quantitative information about the rate of this transformation in Fig. 4. The best fit results for samples 0, 5, 8, 11, 16 and 48 show a gradual and monotonic decrease of the fraction of $Fe_2(MoO_4)_3$ from 99% to 37%. According to these results, the average Fe charge states in all samples vary from +3 for S0 to +2.37 for S48. This result demonstrates that the average Fe oxidation state in all spent catalysts, even for the longest reaction time, is still much higher than +2 which is the oxidation state of Fe in $FeMoO_4$.

Due to the ensemble-averaging nature of XAFS, there are two models that can be used to interpret the PCA results: 1) "homogeneous transformation", in which every Fe atom changes its charge state from +3 to +2.37 (sample S0 to sample S48) and 2) "heterogeneous transformation", where Fe atoms are divided into two groups at all times, with charge states of +3 and +2, with volume fractions x and $1 - x$, respectively. The volume fraction of Fe^{3+} changes from 99% to 37% for samples S0 to S48, respectively. Both models gave identical XANES trends and identical results based on linear combination analysis. Hence, within the results of just one technique, XANES, it is impossible to differentiate between the two models. However, Raman spectra show that Fe^{3+}, in particular $Fe_2(MoO_4)_3$, remains in all of the samples through different reaction stages, not only in the fresh catalyst, S0, but also in the last one, S48. That observation is consistent with model 2) and inconsistent with model 1). Thus, the combination of XAFS and Raman measurements is required to validate a hypothesis of partial $Fe_2(MoO_4)_3$ transformation, specifically $Fe_2(MoO_4)_3 \rightarrow FeMoO_4$ during the selective ammoxidation process. This transformation will be discussed in greater detail below.

3.3. UV-vis diffuse reflectance spectroscopy

Fig. 5 shows the DR-UV-vis spectra of selected samples of Fe–Mo–Bi catalysts at different reaction times. All of the spectra exhibit a characteristic absorption band of $Fe_2(MoO_4)_3$ at ~460 nm.[12,38] The broad absorption in the UV region is ascribed to the presence of both tetrahedral and octahedral oxomolybdate groups,[39] whereas the one in the visual region is attributed to Fe_2O_3.[40] This iron oxide becomes increasingly abundant, accompanied by the catalyst sample showing a red-brown color characteristic of fresh Fe_2O_3,[41] with longer reaction times according to either or both of these mechanisms:

$$3FeMoO_4 + 3/4O_2 \rightarrow Fe_2(MoO_4)_3 + 1/2Fe_2O_3 \quad (1)$$

$$2FeMoO_4 + 1/2O_2 \rightarrow Fe_2O_3 + 2MoO_3 \quad (2)$$

Taking into account the different crystal structures of α- and β-$FeMoO_4$ phases (Mo^{6+} coordination is octahedral in α and tetrahedral in β), it is reasonable to conclude that mechanism (1) occurs preferentially for the β phase and (2) for the α phase, as Mo^{6+} coordination is tetrahedral in $Fe_2(MoO_4)_3$ but octahedral in MoO_3. Given that no MoO_3 was detected in the Raman spectra from S0 through S48, one can further conclude that eqn (1) is the main reoxidation path during the entire catalytic process. As a result, eqn (1) will lead to more stable catalytic activities than eqn (2) due to the regeneration of $Fe_2(MoO_4)_3$. As for the increasing accumulation of Fe_2O_3, as evidenced by the UV-Vis spectra (Fig. 5), its absence in the Raman spectra and in the Fe K-edge XANES spectra indicates that it is present in the sample as a minority Fe species whose volume fraction does not exceed *ca.* 5%, which is the

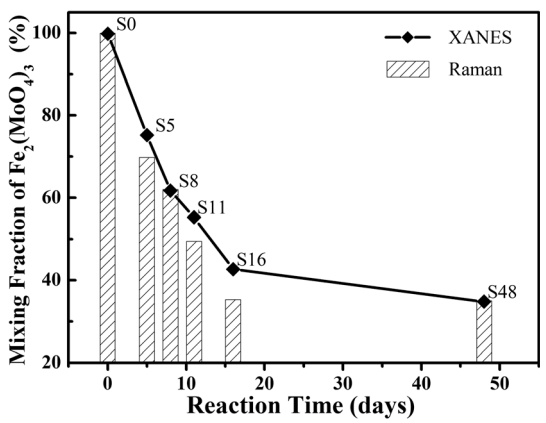

Fig. 4 Fractions of $Fe_2(MoO_4)_3$ in samples S0 through S48 obtained using two different characterization methods, Raman and XANES, exhibit similar trends. The two measurements indicate that the amount of $Fe_2(MoO_4)_3$ has decreased with reaction time.

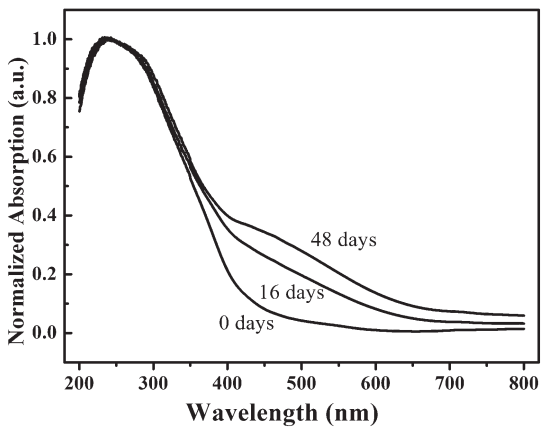

Fig. 5 Diffuse reflectance UV-visible spectra of selected Fe–Mo–Bi catalyst samples. The data were normalized by the absorption maximum. The increasing intensity in the region between 400 and 700 nm shows the increasing amount of Fe_2O_3 with reaction time.

uncertainty in the Fe speciation by principal component analysis of XANES spectra.

4. Discussion

As well documented elsewhere,[42,43] propylene ammoxidation obeys the Mars–van Krevelen mechanism and is a six-electron redox process.[44] Iron molybdate, both ferric and ferrous forms, is a good example of an efficient redox couple. It can promote air–dioxygen dissociation on Fe^{2+} into lattice oxygen, $[O]_L$, and its transfer to the active site using Fe^{3+}.[45] The latter, in turn, will reoxidize the resulting reduced Bi and Mo,[10,46] further turning C_3H_6 into the target product, C_3H_3N:

$$Fe^{2+} + 1/2O_2 \rightarrow Fe^{3+} + [O] + e \quad (3\text{-}1)$$

$$Bi^{0+}(Mo^{4+}) + 3Fe^{3+} \rightarrow Bi^{3+}(Mo^{6+}) + 3Fe^{2+} \quad (3\text{-}2)$$

$$C_3H_6 + NH_3 + 3[O] \rightarrow C_3H_3N + 3H_2O \quad (3\text{-}3)$$

It is evident from these examples that iron molybdate is an active species throughout the entire catalytic reaction and plays crucial roles in the ammoxidation process. To achieve high performance on the Fe–Mo–Bi catalyst, the balance between Fe^{3+} and Fe^{2+} should be kept close to that in the initial state, which is known to have the highest catalytic activity and selectivity.[47] Our experiment demonstrated (Fig. 1) that the initial state of iron molybdate, $Fe_2(MoO_4)_3$, has decomposed significantly for all catalyst samples from S5 through S48. The rate of decomposition was fastest during the first 16 days of the catalytic process.

XAS results not only have revealed the time-dependent decomposition of iron molybdate during the reaction, but also have revealed that the iron-containing phase in the fresh sample, S0, is predominantly $Fe_2(MoO_4)_3$. In addition, the combined use of Raman spectroscopy and XAS helped us to propose the deactivation mechanism for $Fe_2(MoO_4)_3$, which follows the $Fe_2(MoO_4)_3 \rightarrow FeMoO_4$ step. Another important result emerging from this work is that Fe^{3+} directly transforms to Fe^{2+} with no intermediate phase. During this transformation, the volume fraction of Fe^{3+} changes from 100 to 37% for samples S0 to S48, respectively, and the volume fraction of Fe^{2+} increases accordingly. While speciation of the chemical states of iron has been made possible by XAS in earlier studies,[48,49] it is due to the complementarity of XAS and Raman experiments that this conclusion can be made in the present case. Each technique, taken alone, will only show an incomplete picture.

We now turn our attention to the possible origins of decomposition of $Fe_2(MoO_4)_3$. The following equation is a plausible description of the process:

$$Fe_2(MoO_4)_3 \rightleftharpoons 2FeMoO_4 + MoO_3 + 1/2O_2 \quad (4)$$

As an ideal catalyst, iron molybdate could strike a balance between its ferric and ferrous forms during the catalysis process, and the balance should be fully reversible. In that case, the catalytic activity of the spent catalyst, *e.g.*, conversion of propylene, will be same as that of the fresh one. However, due to the loss of MoO_3 *via* volatilization and the much easier sublimation of $MoO_2(OH)_2$ after combination with resulting H_2O (eqn (3)),[50] eqn (4) loses its reversibility. Therefore, ferrous molybdate can only partially get oxidized and restored back to $Fe_2(MoO_4)_3$ incompletely, resulting in an increased amount of the resultant $FeMoO_4$. We propose that eqn (1) is the likely oxidation route because no MoO_3 is detected in the Raman spectra (Fig. 1) and it is accompanied by a small amount of Fe_2O_3 which was detected by DR-UV-Vis spectroscopy (Fig. 5). The presence of a minute amount of iron oxide is not in contradiction with our XAS results because the uncertainties in the LCA-derived error bars on mixing fractions allow for 5% of another iron species in the sample (*vide supra*), and UV-vis is highly sensitive to Fe_2O_3. Hence, the role of the UV-vis measurement is very important here because, without it, the presence of Fe_2O_3 could not have been detected.

In conclusion, based on the observations described above, we find that continuously increasing accumulation of $FeMoO_4$ and depletion of $Fe_2(MoO_4)_3$ is inevitable with the increased reaction time, provided that no additional MoO_3 is added to the reaction mixture to reverse eqn (4) towards the $Fe_2(MoO_4)_3$ direction. As a result, the catalytic performance of the Fe–Mo–Bi catalyst degrades with reaction time.

Two recommendations for rationally designing better ammoxidation catalysts emerged from our findings. First, it is important to maintain a sufficient number of Fe^{3+} sites in an overall reducing atmosphere (propylene ammoxidation to acrylonitrile); it is necessary to stabilize the Fe^{3+} state structurally and/or functionally. One candidate for such stabilizer is the Cr^{3+}/Cr^{2+} redox couple. It is generally more effective at higher temperature than the iron couple;[43] in addition, it acts as a structural diluent to iron and a booster of the Fe^{3+} state in the Fe–Mo–Bi matrix. Relevant tests are presently under way in our group and will be reported elsewhere. Second, it is important to replenish MoO_3 in the reacting mixture to compensate for its loss through volatilization or sublimation to slow down the collapse of ferric molybdate. MoO_3 may come from a separate component compound or some other compound as suggested elsewhere.[5,6]

Based on the discussion stated above, we conclude that ideal Fe–Mo–Bi catalysts for propylene ammoxidation should be both functionally and structurally stable. Functional stability requires that the functional form of iron molybdate should be kept the same as in the fresh catalyst. Based on our results and the work of others, a revised feasible model for a highly active and long-term stable Fe–Mo–Bi catalyst may be proposed, as illustrated in Fig. 6. In this catalyst the Fe^{3+}/Fe^{2+} redox couple is crucial, both to composing reversible redox processes and stabilizing the main structure of catalysts by suppressing its deformation, due to active component decomposition.

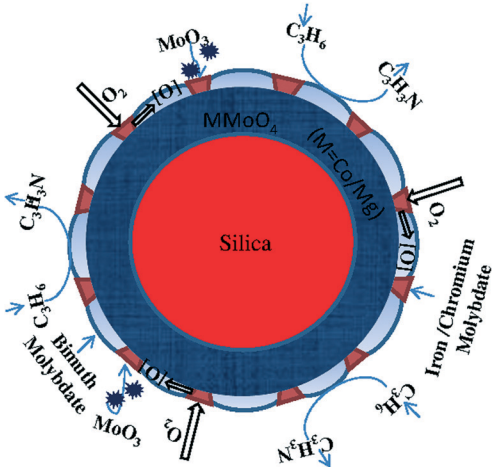

Fig. 6 A schematic model of the Fe–Mo–Bi catalyst showing the role of the Fe^{3+}/Fe^{2+} redox couple during the propylene catalytic ammoxidation process. Propylene, C_3H_6, is converted into the target compound, C_3H_3N, on bismuth molybdate through H-abstraction and lattice O-incorporation, while iron molybdate (including ferric and ferrous) facilitates dioxygen dissociation and lattice oxygen transfer. Two highlighted strategies proposed here are the introduction of the Cr^{3+}/Cr^{2+} redox couple in the catalyst preparation and replenishment of MoO_3 *via* a separate component or compound during the reaction process.

5. Summary and conclusions

In our Fe–Mo–Bi catalysts, an iron molybdate phase identified as $Fe_2(MoO_4)_3$ has undergone dramatic partial (more than 60%) decomposition with increasing reaction time. This decomposition is a one-step transformation from Fe^{3+} into another form of iron molybdate, namely $FeMoO_4$, with an iron charge state of +2. These results were obtained by a combination of Raman spectroscopy and XANES spectroscopy studies of the fresh and spent catalysts at different reaction times. DR-UV-vis measurements revealed a small fraction (less than 5 volume%) of Fe_2O_3 during the reaction process. The combination of these measurements allowed us to propose a mechanism of transformation of iron molybdate and its role in the propylene ammoxidation process. This work highlights the critical role of Fe^{3+} species for the stable and efficient conversion of propylene to acrylonitrile in selective ammoxidation. A modification of the Fe–Mo–Bi catalyst that will help stabilize Fe^{3+} ions is proposed.

Acknowledgements

AIF acknowledges support from the Chemical Sciences, Geosciences, and Biosciences Division, Office of Basic Energy Sciences, Office of Science, U. S. Department of Energy (grant no. DE-FG02-03ER15476). Use of the NSLS is supported by the U.S. Department of Energy, Office of Science, Office of Basic Energy Sciences under contract no. DE-AC02-98CH10886. Beamline X19A at the NSLS is supported in part by the Synchrotron Catalysis Consortium, U.S. Department of Energy (grant no. DE-FG02-05ER15688). We are grateful to Drs. Yuanyuan Li and Nebojsa Marinkovic for their help with synchrotron measurements.

Notes and references

1 R. Grasselli, J. Burrington, D. Buttrey, P. DeSanto Jr., C. Lugmair, A. Volpe Jr. and T. Weingand, *Top. Catal.*, 2003, **23**, 5–22.
2 R. K. Grasselli, *Proceedings of the DGMK Conference*, 2001, Hamburg, Germany, p. 147.
3 T. S. R. P. Rao and K. R. Krishnamurthy, *J. Catal.*, 1985, **95**, 209–219.
4 R. K. Grasselli and H. F. Hardman, *U. S. Patent* 3642930, 1972.
5 R. K. Grasselli, D. D. Suresh and H. F. Hardman, *U. S. Patent* 4001317, 1977; R. K. Grasselli, D. D. Suresh and A. F. Miller, *U. S. Patent* 4167494, 1979.
6 G. W. Keulks, L. D. Krenzke and T. M. Notermann, in *Advances in Catalysis*, ed. H. P. D. D. Eley and B. W. Paul, Academic Press, 1979, vol. 27, pp. 183–225.
7 I. B. Annenkova, T. G. Alkazov and M. S. Belenku, *Kinet. Catal.*, 1969, **10**, 1305–1311.
8 P. A. Batist, C. G. M. van de Moesdijk, I. Matsuura and G. C. A. Schuit, *J. Catal.*, 1971, **20**, 40–57.
9 M. W. J. Wolfs, *Ph.D. thesis*, Selective Oxidation of Olefins over Multicomponent Molybdate Catalysts. Technische Hoge School, Eindhoven 1974; I. Matsuura and M. W. J. Wolfs, *J. Catal.*, 1975, **37**, 174–178.
10 P. A. G. Van Oeffelen, *Ph.D. thesis*, Selective Oxidation of Olefins on Molybdate Catalysts, Technische Hoge School, Eindhoven, 1978.
11 P. A. Batist, *Surf. Technol.*, 1979, **9**, 443–446.
12 M. W. J. Wolfs and P. H. A. Batist, *J. Catal.*, 1974, **32**, 25–36.
13 A. P. V. Soares, M. F. Portela, A. Kiennemann and L. Hilaire, *Chem. Eng. Sci.*, 2003, **58**, 1315–1322.
14 N. Pernicone, *Catal. Today*, 1991, **11**, 85–91.
15 N. Burriesci, F. Garbassi, M. Petrera, G. Petrini and N. Pernicone, in *Studies in Surface Science and Catalysis*, ed. B. Delmon and G. F. Froment, Elsevier, 1980, vol. 6, pp. 115–126.
16 S. Bordiga, E. Groppo, G. Agostini, J. A. van Bokhoven and C. Lamberti, *Chem. Rev.*, 2013, **113**, 1736–1850; I. E. Wachs and C. A. Roberts, *Chem. Soc. Rev.*, 2010, **39**, 5002–5017.
17 R. A. Schoonheydt, *Chem. Soc. Rev.*, 2010, **39**, 5051–5066; F. Cesano, S. Bertarione, A. Piovano, G. Agostini, M. M. Rahman, E. Groppo, F. Bonino, D. Scarano, C. Lamberti, S. Bordiga, L. Montanari, L. Bonoldi, R. Millini and A. Zecchina, *Catal. Sci. Technol.*, 2011, **1**, 123–136.
18 G. Waychunas, M. Apted and G. Brown Jr., *Phys. Chem. Miner.*, 1983, **10**, 1–9.
19 A. Patlolla, P. Baumann, W. Xu, S. D. Senanayake, J. A. Rodriguez and A. I. Frenkel, *Top. Catal.*, 2013, **56**, 896–904.
20 Q. Xu, G. Jia, J. Zhang, Z. Feng and C. Li, *J. Phys. Chem. C*, 2008, **112**, 9387–9393.
21 R. K. Grasselli, *Catal. Today*, 1999, **49**, 141; R. K. Grasselli, *Appl. Catal.*, 1985, **15**, 127–139.

22 D. D. Suresh, M. S. Friedrich and M. J. Seely, *U. S. Patent* 5212137, 1993; O. V. Udalova, D. P. Shashkin, M. D. Shibanova and O. V. Krylov, *Kinet. Catal.*, 2005, **46**, 535–544.

23 B. Ravel and M. Newville, *J. Synchrotron Radiat.*, 2005, **12**, 537–541.

24 S. R. Wasserman, *J. Phys. IV*, 1997, **7**, C2-203–205.

25 A. I. Frenkel, O. Kleifeld, S. R. Wasserman and I. Sagi, *J. Chem. Phys.*, 2002, **116**, 9449–9456.

26 P. Delichere, A. Hugot-Le Goff and S. Joiret, *Surf. Interface Anal.*, 1988, **12**, 419–423.

27 I. Kanesaka, H. Hashiba and I. Matsuura, *J. Raman Spectrosc.*, 1988, **19**, 213–218.

28 H. Tian, I. E. Wachs and L. E. Briand, *J. Phys. Chem. B*, 2005, **109**, 23491–23499; I. Matsuura, R. Schut and K. Hirakawa, *J. Catal.*, 1980, **63**, 152–166.

29 G. Hill Jr and J. H. Wilson III, *J. Mol. Catal.*, 1990, **63**, 65–94.

30 X. Ge, J. Shen and H. Zhang, *Sci. China, Ser. B: Chem.*, 1996, **39**, 53–63.

31 M. Dieterle, G. Weinberg and G. Mestl, *Phys. Chem. Chem. Phys.*, 2002, **4**, 812–821.

32 J. Shirakawa, M. Nakayama, M. Wakihara and Y. Uchimoto, *J. Phys. Chem. B*, 2007, **111**, 1424–1430.

33 A. M. Beale, S. D. M. Jacques, E. Sacaliuc-Parvalescu, M. G. O'Brien, P. Barnes and B. M. Weckhuysen, *Appl. Catal., A*, 2009, **363**, 143–152.

34 C. C. Torardi and E. Prince, *Mater. Res. Bull.*, 1986, **21**, 719–726.

35 A. W. Sleight, B. L. Chamberland and J. F. Weiher, *Inorg. Chem.*, 1968, **7**, 1093–1098.

36 J. Y. Kim, J. A. Rodriguez, J. C. Hanson, A. I. Frenkel and P. L. Lee, *J. Am. Chem. Soc.*, 2003, **125**, 10684–10692.

37 S. R. Wasserman, P. G. Allen, D. K. Shuh, J. J. Bucher and N. M. Edelstein, *J. Synchrotron Radiat.*, 1999, **6**, 284–286.

38 P. Forzatti, P. L. Villa, N. Ferlazzo and D. Jones, *J. Catal.*, 1982, **76**, 188–207.

39 W. D. Kovats and C. G. Hill, *Appl. Spectrosc.*, 1986, **40**, 1215–1223.

40 A. C. Scheinost, A. Chavernas, V. Barron and J. Torrent, *Clays Clay Miner.*, 1998, **46**, 528–536.

41 Z. Zhang, M. F. Hossain and T. Takahashi, *Appl. Catal., B*, 2010, **95**, 423–429.

42 R. K. Grasselli, *J. Chem. Educ.*, 1986, **63**, 216–221.

43 P. Mars and D. W. van Krevelen, *Chem. Eng. Sci.*, 1954, **3**, 41–59.

44 R. K. Grasselli, Ammoxidation, in *Handbook of Heterogeneous Catalysis*, ed. G. Ertl, J. Weitkamp, and H. Knoezinger, John Wiley & Son Inc., New York, 1997, vol. 5, p. 2302.

45 R. K. Grasselli, *Catal. Today*, 1999, **49**, 141–153.

46 R. Schlögl, A. Knop-Gericke, M. Hävecker, U. Wild, D. Frickel, T. Ressler, R. E. Jentoft, J. Wienold, G. Mestl, A. Blume, O. Timpe and Y. Uchida, *Top. Catal.*, 2001, **15**, 219–228.

47 A. A. Firsova, Y. V. Maksimov, V. Y. Bychkov, O. V. Isaev, I. P. Suzdalev and V. N. Korchak, *Kinet. Catal.*, 2000, **41**, 116–121.

48 E. Borfecchia, L. Mino, D. Gianolio, C. Groppo, N. Malaspina, G. Martinez-Criado, J. A. Sans, S. Poli, D. Castelli and C. Lamberti, *J. Anal. At. Spectrom.*, 2012, **27**, 1725–1733.

49 G. Berlier, G. Spoto, S. Bordiga, G. Ricchiardi, P. Fisicaro, A. Zecchina, I. Rossetti, E. Selli, L. Forni, E. Giamello and C. Lamberti, *J. Catal.*, 2002, **208**, 64–82.

50 L. Zhang, D. Liu, B. Yang and J. Zhao, *Appl. Catal., A*, 1994, **117**, 163–171.